

# Supplementary Information for “Controlled catch and release of microwave photon states”

Yi Yin,<sup>1,\*</sup> Yu Chen,<sup>1</sup> Daniel Sank,<sup>1</sup> P. J. J. O’Malley,<sup>1</sup> T. C. White,<sup>1</sup> R. Barends,<sup>1</sup> J. Kelly,<sup>1</sup> Erik Lucero,<sup>1</sup> Matteo Mariantoni,<sup>1,2</sup> A. Megrant,<sup>3</sup> C. Neill,<sup>1</sup> A. Vainsencher,<sup>1</sup> J. Wenner,<sup>1</sup> Alexander N. Korotkov,<sup>4</sup> A. N. Cleland,<sup>1,2</sup> and John M. Martinis<sup>1,2,†</sup>

<sup>1</sup>*Department of Physics, University of California, Santa Barbara, CA 93106, USA*

<sup>2</sup>*California NanoSystems Institute, University of California, Santa Barbara, CA 93106, USA*

<sup>3</sup>*Department of Materials, University of California, Santa Barbara, CA 93106, USA*

<sup>4</sup>*Department of Electrical Engineering, University of California, Riverside CA 92521, USA*

---

\* Present address: Department of Physics, Zhejiang University, Hangzhou 310027, China.

† martinis@physics.ucsb.edu

## I. SAMPLE FABRICATION

The device was fabricated using conventional photolithography and plasma etching on a multilayered structure. The resonator was made from a sputtered 150 nm-thick superconducting aluminum base film on a sapphire substrate. The phase qubit and the superconducting quantum interference device (SQUID) in the variable coupler were made using Al/AlO<sub>x</sub>/Al Josephson junctions. A low-loss dielectric, hydrogenated amorphous silicon, was used as the insulator in capacitors and wiring crossovers.

## II. EXPERIMENTAL SETUP AND CONTROL ELECTRONICS

A detailed schematic of the resonator control and measurement system is shown in Fig. S1a. The microwave excitation signal for the resonator is generated by mixing a digitally-synthesized intermediate frequency (IF) signal with a microwave frequency local oscillator (LO). The I and Q quadratures of the IF signal were generated using a field-programmable gate array (FPGA) and a customized 2-channel 14-bit digital-to analog converter (DAC). The RF output of the mixer was sent into the cryostat and routed through a circulator to the variable coupler and resonator. Microwave signals from the resonator were routed by the circulator to a cryogenic amplifier  $G$  with 35 dB of gain and a noise temperature of 4 K. After further room-temperature amplification (60 dB of gain), the output signal was mixed down with the same local oscillator (LO) signal as the up-converter, generating the same IF (sideband) frequency. The  $I$  and  $Q$  quadratures were digitized at 500 megasamples/second using a 2-channel 8-bit analog-to-digital converter (ADC), and the signal passed to another FPGA for further processing. In the “oscilloscope mode”, the digitized signals were sent directly to a computer without further processing, as shown in the time-trace data in Fig. 3 and Fig. 4 in the main text. In the “demodulation mode”, the  $I$  and  $Q$  signals were multiplied by sine and cosine waveforms at the sideband frequency and summed in real time. The continuous summation signal guarantees rapid fast Fourier transform (FFT) processing once the data acquisition is complete; this was used for the data in Fig. 4b in the main text.

Qubit control used a system similar to that for the resonator. The microwave pulses for qubit control ( $x/y$  rotations) were generated by mixing a continuous microwave signal and a shaped quasi-d.c. waveform from a 2-channel 14-bit digital-to-analog converter (DAC).

Another quasi-d.c. pulse generator controls qubit  $z$ -axis rotations and measurement.

Figure 1 in the main text shows the circuit for the experiment. The variable coupler is connected a distance  $d = 0.3$  mm from the grounded end of the  $\lambda/4$  coplanar waveguide resonator (4.8 mm long). The coupler consists of a transformer with inductances  $L_1$ ,  $L_2$  and a negative mutual inductance  $M$ . The positive mutual inductance from the dc SQUID is  $L_s = \Phi_0/4\pi I_c |\cos(\pi\Phi/\Phi_0)|$ , where  $I_c = 1.6 \mu\text{A}$  is the critical current of the junction,  $\Phi$  the applied magnetic flux and  $\Phi_0 = h/2e$  the magnetic flux quantum. The characteristic impedances of the microwave resonator and the transmission line are  $Z_r = 80 \Omega$  and  $Z_0 = 50 \Omega$  respectively.

### III. THEORETICAL MODELING OF RESONATOR $T_1$

Using an equivalent electrical circuit for the variable coupling experiment, shown in Fig. S2a, we calculate the expected resonator  $T_1$  due to coupling to the external  $50 \Omega$  transmission line. We also calculate the small effect this coupling has on the resonance frequency of the resonator. Both calculations compare well with experiment.

We replace the short portion ( $\sim \lambda/60$ ) of the resonator between the coupler connection and the resonator ground with an effective inductance  $L_e$ , and the transformer and coupling circuit with an equivalent  $L'_1$ ,  $L'_2$  and mutual inductance  $M'$ , with  $L'_2$  connected to an infinite transmission line with characteristic impedance  $Z_0$ . We calculate the resonator reflection and transmission amplitudes  $\mathbf{r}$  and  $\mathbf{t}$ .

The effective inductances  $L'_1$ ,  $L'_2$  and inductance  $M'$  are given by

$$L'_1 = L_1 + L_s, \quad L'_2 = L_2 + L_s, \quad M' = M + L_s. \quad (2)$$

The coupler is turned off when  $M' = 0$ . Note that because all the equivalent inductances include  $L_s$ , modulating  $M'$  by changing  $L_s$  modulates  $L'_1$  and  $L'_2$  as well:

$$L'_1 = (L_1 - M) + M', \quad L'_2 = (L_2 - M) + M'. \quad (3)$$

To calculate the inductance  $L_e$ , which represents the small length of resonator from the coupling point to ground, we impose a voltage  $Ae^{i\omega t}$  in the resonator traveling from the open (qubit) end towards the coupler end, and approximate the reflected voltage as  $-Ae^{i\omega t}$

(ignoring the portion transmitted into the transmission line). The voltage at distance  $d$  from the grounded end is  $V = Ae^{i\omega t}(e^{i\omega d/c} - e^{-i\omega d/c}) = 2iAe^{i\omega t}\sin(\omega d/c)$ , with  $c$  the phase velocity of light in the resonator. The current at this point is  $I = Ae^{i\omega t}(e^{i\omega d/c}/Z_r + e^{-i\omega d/c}/Z_r) = 2(A/Z_r)e^{i\omega t}\cos(\omega d/c)$ , so the wave impedance is  $Z = V/I = iZ_r \tan(\omega d/c) = i\omega L_e$ , yielding the effective inductance

$$L_e = \frac{Z_r}{\omega} \tan\left(\frac{\omega d}{c}\right) = \frac{Z_r}{\omega} \tan\left(\frac{2\pi d}{\lambda}\right) \quad (4)$$

(note this is evaluated at  $\omega = 2\pi f_r$ , the resonator frequency).

The calculation of the transmission and reflection amplitudes  $\mathbf{t}$  and  $\mathbf{r}$  is similar to the derivation in [1]. Assume a voltage with amplitude  $A$  is incident on the coupler from the left side of the resonator, with reflected voltage  $\mathbf{r}A$  and voltage transmitted into the transmission line  $\mathbf{t}A$ . The voltage across  $L'_1$  is  $V = (1 + \mathbf{r})A$ , while the voltage across  $L'_2$  is denoted by  $x = \mathbf{t}A$ . The currents flowing into  $L'_1$  and  $L'_2$  are  $I_1 = (1 - \mathbf{r})A/Z_r - V/(i\omega L_e)$  and  $I_2 = -x/Z_0$ , respectively. Using currents  $I_1$  and  $I_2$ , we write equations for the voltage amplitudes  $x$  and  $V$ :

$$\begin{aligned} x &= i\omega M' \left[ \frac{(1 - \mathbf{r})A}{Z_r} - \frac{(1 + \mathbf{r})A}{i\omega L_e} \right] - i\omega L'_2 \frac{x}{Z_0}, \\ (1 + \mathbf{r})A &= i\omega L'_1 \left[ \frac{(1 - \mathbf{r})A}{Z_r} - \frac{(1 + \mathbf{r})A}{i\omega L_e} \right] - i\omega M' \frac{x}{Z_0}. \end{aligned} \quad (5)$$

From these equations, we can calculate the reflection amplitude  $\mathbf{r}$  and transmission amplitude  $\mathbf{t} = x/A$  (note that  $|\mathbf{t}|^2 Z_r/Z_0 + |\mathbf{r}|^2 = 1$ ):

$$\begin{aligned} a &\equiv \frac{1 + \mathbf{r}}{1 - \mathbf{r}} = \frac{\frac{i\omega L'_1}{Z_r} + \frac{\omega^2 M'^2}{Z_r Z_0 (1 + i\omega L'_2/Z_0)}}{1 + \frac{L'_1}{L_e} - \frac{i\omega M'^2}{Z_0 L_e (1 + i\omega L'_2/Z_0)}}, \\ \mathbf{r} &= - \left( \frac{1 - a}{1 + a} \right), \\ \mathbf{t} &= i \frac{2\omega M'}{1 + a} \left( \frac{1}{Z_r} + \frac{ia}{\omega L_e} \right) \frac{1}{1 + i\omega L'_2/Z_0}. \end{aligned} \quad (6)$$

In the limit  $\omega L_e \ll Z_r$  and  $\omega M' \ll Z_0$ , which apply here, the reflection and transmission

amplitudes can be approximated as

$$\begin{aligned}\mathbf{r} &\approx -1 + 2a \approx -1 + i \frac{2\omega L_e L'_1}{Z_r(L'_1 + L_e)}, \\ \mathbf{t} &\approx i \frac{2\omega L_e M'}{Z_r(L'_1 + L_e)} \frac{1}{1 + i\omega L'_2/Z_0}.\end{aligned}\quad (7)$$

The decay time of the resonator is obtained from the transmission amplitude [1]:

$$1/\kappa_c = \frac{Q}{\omega} \approx \frac{\pi}{\omega|\mathbf{t}|^2} \frac{Z_0}{Z_r} = \frac{\pi Z_r Z_0 (L'_1 + L_e)^2 (1 + \omega^2 L'_2{}^2/Z_0^2)}{4\omega^3 L_e^2 M'^2}, \quad (8)$$

where  $\omega = 2\pi f_r$  is the resonator frequency.

The coupler bias dependence of the resonator  $T_1$  is extracted from the data in the main text and shown in Fig. S2b (blue dots). The predicted  $T_1$  from Eq. (8), using the actual circuit parameters, is also displayed in Fig. S2b (red line), in good agreement with the data. We note that the inductive coupling changes sign when the coupler strength sweeps through zero coupling [2, 3], verified by the expected  $\pi$  phase change in a Wigner tomography measurement (see next section and Fig. S3e).

The resonant frequency of the  $\lambda/4$  resonator is primarily determined by the resonator length and characteristic impedance, but is also affected by the variable coupler. The change in resonance frequency with coupler bias can be measured experimentally, and verified by the following calculation: Compared to the frequency  $f_r$  at zero coupling ( $M' = 0$ ), the resonance frequency shifts by  $\Delta f$ ,

$$\Delta f \approx -\frac{4f_r^2 L_e^2 M'}{\pi^2 Z_r (L_e + L_1 - M)(L_e + L_1 - M + M')}. \quad (9)$$

We compare the coupler bias dependence of  $f_r$ , measured spectroscopically, with the frequency tuning from Eq. (9), in Fig. S2c. The frequency tunes over  $\sim 15$  MHz, a very small fraction of the resonator frequency. Previous experiments have demonstrated resonator frequency tuning using Josephson junctions or SQUIDs embedded in a resonator [4, 5]. Here the frequency tuning is quite small, and is a by-product of the variable coupler located outside the resonator.

We have measured the coupling dependence of the one-photon decay in Fig. 2b in the main text with a fast coupler bias. For comparison, a similar measurement was performed

using the slow coupler bias, with data shown in Fig. S2d. The bias range is expanded to show the periodic response of the lifetime to the coupler flux bias.

#### IV. CHARACTERIZATION OF RESONATOR STATES USING SWAP SPECTROSCOPY AND WIGNER TOMOGRAPHY

We measured the single photon lifetime  $T_1$  to characterize the coupling strength, as discussed in the main text. We also used swap spectroscopy to perform an equivalent characterization, shown here with the coupler set to two representative coupling strengths. The pulse sequence is shown in Fig. S3a, starting with the system initialized in the ground state. The de-tuned qubit was excited by a  $\pi$  pulse to  $|e\rangle$  and then tuned close to resonance with the resonator, using a qubit tuning  $z$ -pulse with variable amplitude. The variable coupler was either left at zero coupling ( $\kappa_{\text{zero}}$ ), or switched to a coupling  $\kappa_c = 1/(30 \text{ ns})$  immediately after tuning the qubit. In either case, the coupling strength was fixed for the full qubit-resonator interaction time  $\tau$ . The qubit excitation probability  $P_e$  was then measured using a triangular measurement pulse.

The qubit excited state probability  $P_e$  is plotted versus the interaction time  $\tau$  and the qubit  $z$ -pulse amplitude in Fig. S3b and c, for weak and strong coupling, respectively. The chevron pattern due to the qubit-resonator photon swapping is evident in Fig. S3b, from which we calibrate the iSWAP [6] pulse amplitude and duration. In contrast, the response in Fig. S3c shows a rapid qubit-resonator relaxation, with energy strongly dissipated into the transmission line. We also note that the center of the chevron pattern in Fig. S3c shifts in comparison to Fig. S3b, due to the resonator frequency shift with coupler strength (Fig. S2c).

The coupling strength changes sign when the coupler bias sweeps through the zero coupling point. An indirect phase-sensitive method, Wigner tomography [7], was used to detect this coupling sign change. The pulse sequence is shown in Fig. S3d. The resonator was prepared in the superposition  $(|0\rangle + |1\rangle)/\sqrt{2}$  state, and then driven by a variable-amplitude classical Gaussian microwave tomography pulse. The coupler was set to two different values during the tomography pulse, such that the coupling strength  $\pm\kappa_c$  had the same amplitude but opposite signs. The microwave tomography pulse, passing through the coupler, displaces and rotates the resonator state in the resonator phase space; the opposite coupling signs give opposite rotation directions to the resonator state for the same tomography pulse. The qubit

was then tuned on-resonance with the resonator for a variable time  $\tau$ , after which the qubit state was measured. Measurements of the qubit excitation probability  $P_e(\tau)$  were analyzed to yield the Fock state probability  $P_n(\alpha)$ , where  $\alpha$  is the complex amplitude and phase of the tomography pulse. The Wigner quasi-probability distribution  $W(\alpha)$  was calculated by evaluating the parity  $W(\alpha) = \sum (-1)^n P_n(\alpha)$ .

The Wigner functions measured with the two signs of coupling strength  $\pm\kappa_c$  are shown in Fig. S3e. The Wigner functions clearly show a relative rotation angle of  $\sim \pi$ . The density matrices of the resonator states can be calculated from the Wigner functions and projected onto the number basis  $\rho_{mn} = \langle m|\rho|n\rangle$ , shown in the lower sub-panel of Fig. S3e. Here, we represent each element in the density matrix by an arrow, whose length and direction correspond to the magnitude and phase of  $\rho_{mn}$ . The direction of the arrow for  $\rho_{01}$  ( $\rho_{10}$ ) contains the relevant phase information, showing a  $\approx \pi$  phase shift with a small phase error of  $9.5^\circ$ .

## V. CALIBRATION OF TRAPPED COHERENT STATE PHOTONS

When a microwave Gaussian pulse with amplitude  $\alpha$  and duration  $t_d$  is used to create a coherent photon state in the resonator, the state can be probed with a qubit through an on-resonance interaction, by measuring the qubit excited state probability  $P_e(\tau)$  as a function of the interaction time  $\tau$ . The photon state probability distribution  $P_n(\alpha)$  can be resolved in the Fock number basis  $|n\rangle$  by decomposing  $P_e(\tau)$  into its discrete Fourier components  $f_n = n f_1$ , where  $f_1 = g/\pi$  is the vacuum Rabi frequency [7].

We used this measurement to calibrate the coherent state stored in the resonator for different coupling strengths and different microwave drive amplitudes  $\alpha$ , with a fixed duration. In Fig. S4a we set the coupler strength to one of two values  $\kappa_c \simeq 1/(3000 \text{ ns})$  and  $\kappa_c \simeq 1/(210 \text{ ns})$ , after which we excited the resonator with a variable amplitude Gaussian microwave pulse, and measured the qubit after a qubit-resonator interaction time  $\tau$ . The top sub-panel shows the pulse sequence, the middle sub-panel the qubit excitation probability  $P_e$  as a function of the microwave pulse amplitude and interaction time  $\tau$  for the smaller coupler strength, and the bottom sub-panel the same measurement for the larger coupler strength. A horizontal line cut (not displayed) shows a periodic but low amplitude oscillation for small drive amplitude  $\alpha$ , transforming to a clear ringing-collapse-revival pattern for

larger  $\alpha$ . When the coupler is set to a small coupling (middle sub-panel of Fig. S4a), it is hard for the microwave source to excite the resonator but the resonator has a large  $T_1$  for trapped photons. When the coupler is instead set to a large coupling (bottom sub-panel of Fig. S4a), photons enter the resonator easily yielding a larger excitation amplitude, but the lifetime is shorter, illustrated by the rapid decay for larger  $\tau$ .

To achieve both long photon lifetimes and low-power excitation, we instead set the coupler to a large value during the microwave drive pulse, then set the coupling to zero to trap the photons during the qubit measurement (Fig. S4b). A representative qubit-resonator interaction measurement for a coherent resonator state is shown in the middle sub-panel of Fig. S4b, with the coupler set to  $\kappa_c \simeq 1/(700 \text{ ns})$  during the microwave excitation pulse. We performed a series of measurements with varying coupling strengths, which were analyzed to give the photon distribution  $P_n(\alpha)$ . For a fixed microwave pulse amplitude ( $\alpha = 1.0$  in the vertical axis of Fig. S4b), we calculated the average photon number  $\langle n(\alpha) \rangle = \sum_m n P_n(\alpha)$ . We display  $\langle n \rangle$  as a function of coupler drive amplitude in the bottom sub-panel of Fig. S4b; this is the calibration method used for the experiment shown in Fig. 3 in the main text.

- 
- [1] Korotkov, A. N. Flying microwave qubits with nearly perfect transfer efficiency. *Phys. Rev. B* **84**, 014510 (2011).
- [2] Hime, T. *et al.* Solid-state qubits with current-controlled coupling. *Science* **314**, 1427–1430 (2006).
- [3] van der Ploeg, S. H. W. *et al.* Controllable coupling of superconducting flux qubits. *Phys. Rev. Lett.* **98**, 057004 (2007).
- [4] Sandberg, M. *et al.* Tuning the field in a microwave resonator faster than the photon lifetime. *Appl. Phys. Lett.* **92**, 203501 (2008).
- [5] Placios-Laloy, A. *et al.* Tunable resonators for quantum circuits. *J. Low Temp. Phys.* **151**, 1034 (2008).
- [6] Martinis, John M. Superconducting Phase Qubits. *Quantum Information Processing* **8**, 81 (2009).
- [7] Hofheinz, M. *et al.* Synthesising arbitrary quantum states in a superconducting resonator. *Nature* **459**, 546–549 (2009).

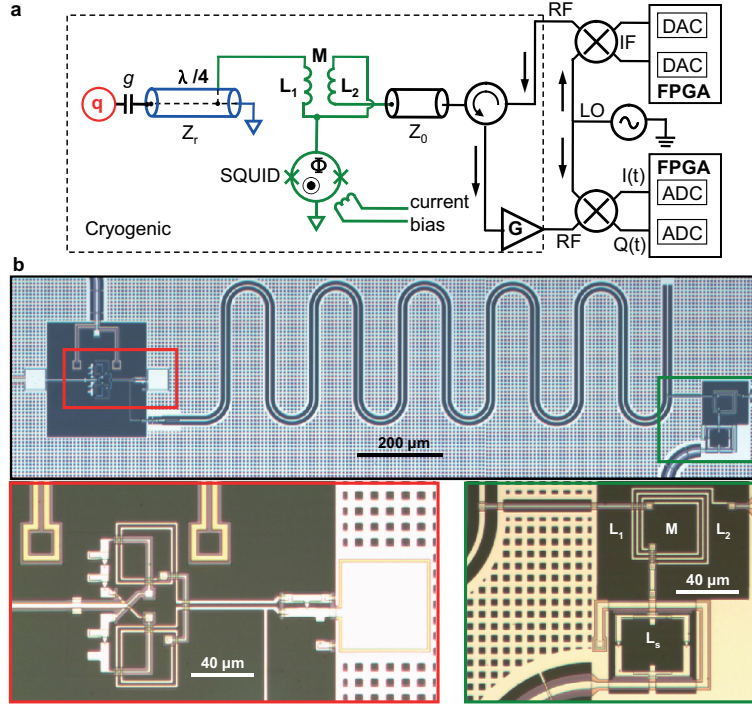


FIG. S1. Experimental setup. **a**, Full schematic for resonator control and measurement electronics. Qubit  $q$  is coupled with coupling strength  $g$  to  $\lambda/4$  resonator with characteristic impedance  $Z_r$ . Other end of resonator is grounded, with variable coupler connected a distance  $\lambda/60$  from grounded end. Variable coupler comprises two inductances  $L_1 = L_2 = 480$  pH with a negative mutual inductance  $M = -138$  pH, and a SQUID with tunable inductance  $L_s(\Phi)$ . Current bias to the flux line to the SQUID controls the SQUID inductance and thus the variable coupler. The coupler is connected to a transmission line with characteristic impedance  $Z_0$ , whose other end is connected through a circulator to a microwave excitation and measurement system (see text for details). **b**, Micrograph of device (top), with details of phase qubit (bottom left) and variable coupler (bottom right).

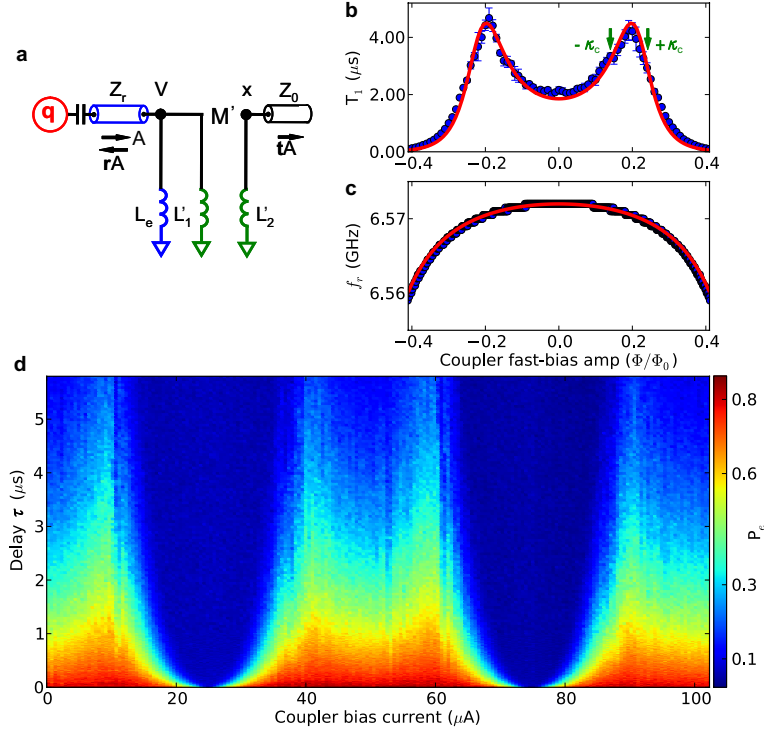


FIG. S2. Modeling of resonator lifetime  $T_1$  and resonance frequency  $f_r$ . **a**, Simplified schematic diagram of the variable coupler end of the resonator. The section of the  $\lambda/4$  resonator between the coupler and ground is approximated by an inductance  $L_e$ , and the transformer is replaced by two effective inductances  $L'_1, L'_2$  with mutual inductance  $M'$ . When a voltage signal with amplitude  $A$  travels from the left side of the resonator to the coupler, the wave is reflected from the coupler as  $rA$  and transmitted in the transmission line as  $tA$ . **b**, Blue dots are the experimental resonator lifetime  $T_1$  extracted from the data shown in the main text in Fig. 2b. Theoretical evaluation of  $T_1$  from Eq. (8) using the circuit design parameters is displayed as a red line. **c**, The resonator frequency  $f_r$  as a function of coupler bias amplitude from spectroscopic measurements (blue dots) and compared with the theoretical prediction (Eq. 9). Arrows indicate coupling  $\pm\kappa_c$  used for Wigner tomography in Fig. S3, with the sign of  $\kappa$  denoting polarity of the inductive coupling. **d**, One-photon decay measurement, similar to Fig. 2b in the main text, but using a slow coupler bias. The periodic response of the lifetime to the coupler current bias is evident.

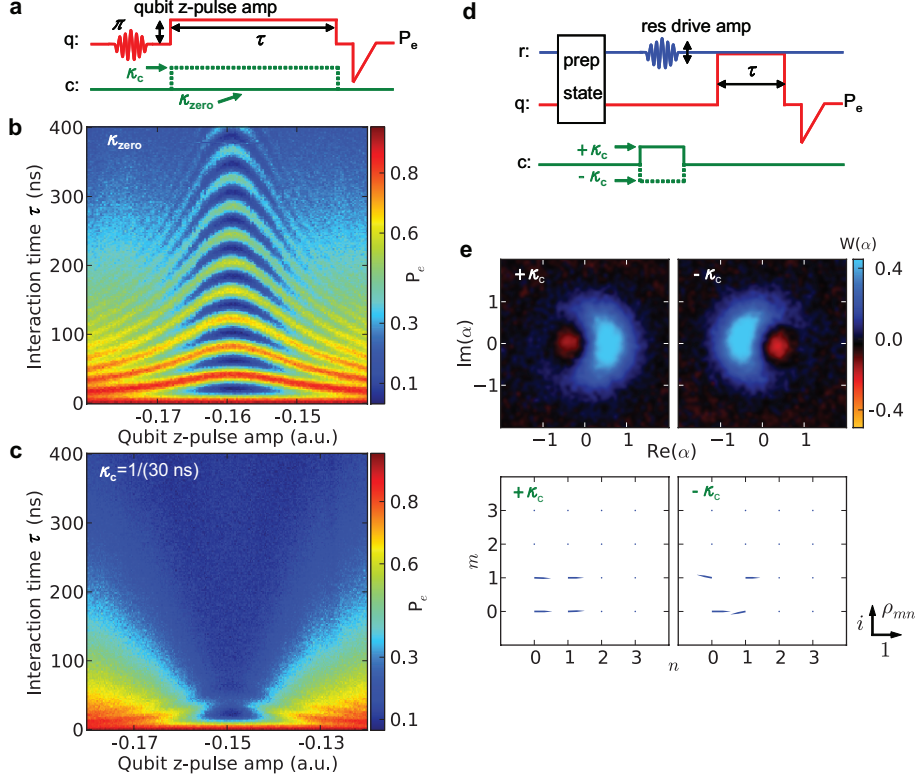


FIG. S3. Swap spectroscopy and Wigner tomography at different coupler biases. **a**, Pulse sequence for swap spectroscopy at two coupler settings. The qubit is excited to  $|e\rangle$  with a  $\pi$  pulse and the excitation swapped to the resonator. The coupler is either left at zero coupling when the qubit is tuned on-resonance with the resonator, or switched immediately to  $\kappa_c = 1/(30 \text{ ns})$ . After a qubit-resonator interaction time  $\tau$ , the qubit excited state probability  $P_e$  is measured. **b**, Measured qubit probability  $P_e$  for swap spectroscopy as a function of qubit  $z$ -pulse amplitude (detuning) and interaction time  $\tau$ , with the resonator coupling to transmission line set to zero. The chevron pattern representing qubit-resonator photon swapping is clearly visible. **c**, In contrast, when the coupler is set to strong coupling  $\kappa_c = 1/(30 \text{ ns})$ , swap spectroscopy shows a rapid energy dissipation and a slight resonant frequency shift. **d**, Pulse sequence for Wigner tomography. The box labeled “prep state” represents resonator preparation in the state  $(|0\rangle + |1\rangle)/\sqrt{2}$ . The coupler is set to zero coupling during the entire sequence except when the microwave source drives the resonator for the tomographic analyzer pulse. During the tomographic pulse, the coupler is set to the same coupling strength but with opposite sign  $\pm\kappa_c = \pm 1/(2000 \text{ ns})$ . Following the tomographic pulse the qubit is used to measure the resonator state. **e**, Wigner functions  $W(\alpha)$  (upper sub-panels) for the  $(|0\rangle + |1\rangle)/\sqrt{2}$  resonator state, plotted as a function of the microwave tomography complex amplitude  $\alpha$  in photon number units (51 by 51 pixels). We calculate density matrices (lower sub-panels) from each Wigner function. The negative sign for the coupling strength introduces a  $\pi$  phase shift between the tomography pulse-induced state rotations, with a small phase error of  $9.5^\circ$ .

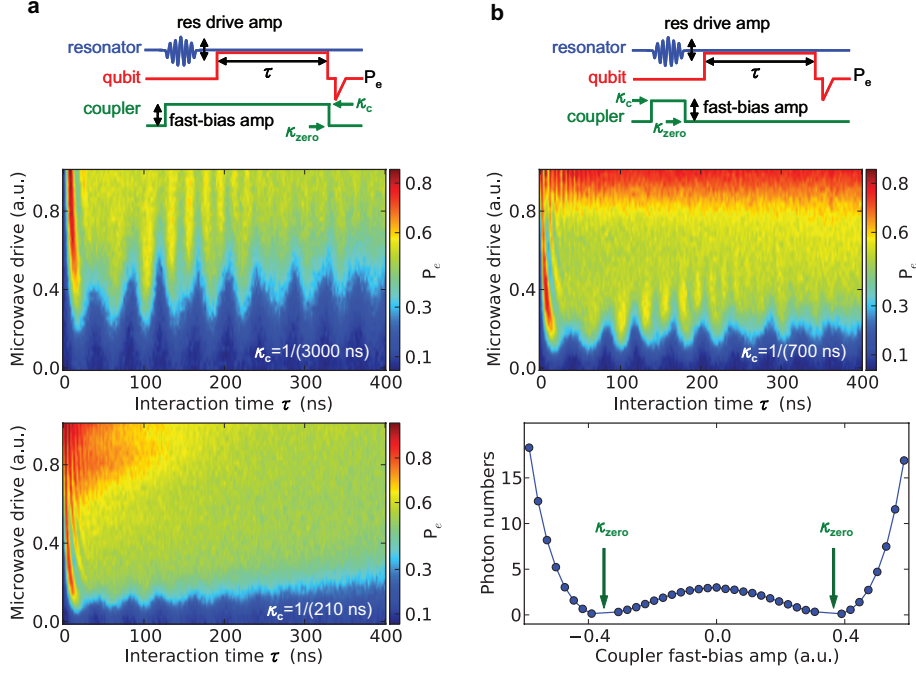


FIG. S4. Calibration of coherent state generation for different coupler strengths. **a**, Top sub-panel: Pulse sequence to generate a resonator coherent state and then perform a qubit measurement. This measurement was performed for two different coupling strengths,  $\kappa_c \simeq 1/(3000 \text{ ns})$  and  $\kappa_c \simeq 1/(210 \text{ ns})$ , with the coupler set to this value prior to the excitation pulse and left at this value during the qubit-resonator interaction. Data in bottom two panels show the qubit excited state probability  $P_e$  versus interaction time  $\tau$  and microwave drive amplitude. The Gaussian microwave pulse was 12 ns in duration (6 ns FWHM) for both panels a and b. **b**, Top sub-panel: Pulse sequence to generate a resonator coherent state with a coupling strength  $\kappa_c \simeq 1/(700 \text{ ns})$ , with the coupling strength set to zero during the subsequent qubit-resonator interaction. Middle panel shows the qubit  $P_e$  as a function of interaction time  $\tau$  and microwave drive amplitude. A population analysis yields the average trapped photon number  $\langle n \rangle$  for different coupling strengths during the microwave drive pulse, shown in the bottom sub-panel, for a microwave drive amplitude  $\alpha = 1.0$ , the same as 1.0 in the vertical axis of the middle sub-panel. Coupler biases yielding zero average photon number are marked by arrows.